Wavelet multiresolution analysis of the three vorticity components in a turbulent far wake

T. Zhou,[1,*] A. Rinoshika,[2] Z. Hao,[1] Y. Zhou,[3] and L. P. Chua[1]
[1]*School of Mechanical and Aerospace Engineering, Nanyang Technological University, Singapore 639798*
[2]*Department of Mechanical Systems Engineering, Yamagata University 4-3-16 Jonan, Yonezawa-shi, Yamagata 992-8510, Japan*
[3]*Department of Mechanical Engineering, The Hong Kong Polytechnic University Hung Hom, Kowloon, Hong Kong, China*
(Received 25 July 2005; revised manuscript received 1 December 2005; published 9 March 2006)

The main objective of the present study is to examine the characteristics of the vortical structures in a turbulent far wake using the wavelet multiresolution technique by decomposing the vorticity into a number of orthogonal wavelet components based on different central frequencies. The three vorticity components were measured simultaneously using an eight-wire probe at three Reynolds numbers, namely 2000, 4000, and 6000. It is found that the dominant contributions to the vorticity variances are from the intermediate and relatively small-scale structures. The contributions from the large and intermediate-scale structures to the vorticity variances decrease with the increase of Reynolds number. The contributions from the small-scale structures to all three vorticity variances jump significantly when Reynolds number is changed from 2000 to 4000, which is connected to previous observations in the near wake that there is a significant increase in the generation of small-scale structures once the Reynolds number reaches about 5000. This result reinforces the conception that turbulence "remembers" its origin.

DOI: 10.1103/PhysRevE.73.036307 PACS number(s): 47.27.wb, 47.32.C−

I. INTRODUCTION

Flow around a circular cylinder is of significant importance for engineering applications. Therefore, the study of this flow has attracted significant attention for many decades. However, our knowledge on this flow is at best empirical [1], even though our understanding on the turbulent wake has been greatly improved in the last two decades due mainly to the successful development of experimental and numerical techniques and various schemes for educing vortical structures. It is now well established that turbulence depends significantly on the initial conditions in the near wake. Even in the far wake, turbulence does not entirely "forget" its origin (e.g., initial conditions) and the self-preservation state in the far region is not strictly achieved [2–4]. The studies by Bonnet *et al.* [5] and George [6] have confirmed that detailed behavior of a turbulent far wake depends significantly on its initial conditions.

The Reynolds number Re ($\equiv U_\infty d/\nu$, where U_∞ is the free stream velocity, d is the diameter of the cylinder and ν is the kinematic viscosity of the fluid) also has a significant effect on the near-wake dynamics. This effect has been studied by a number of investigators in the literature with various degrees of details, including the measurements of mean base pressure, fluctuating lift, vortex formation length, and topology [7–11]. Roshko [12] first found that the two-dimensional periodic vortex street undergoes a transition to three-dimensionality involving two modes of formation of streamwise vorticity in the near wake. At Re=180, mode *A* vortex shedding occurs, characterized by regular streamwise vortices with spanwise wavelength of approximately 3 to 4 cylinder diameters. At Re=230, mode *B* appears, consisting of a more irregular array of rib-like streamwise structures with the mean spanwise wavelength of about one cylinder diameter.

Particular attention has been focused on the study of vortical structures over the Reynolds number range of 10^3-10^4. In this range, the Strouhal number and the drag coefficient of a circular cylinder are approximately constant. However, there is a large change in the formation length of the Karman vortices and the mean base pressure coefficient increases significantly. The velocity fluctuation in the shear layer close to the cylinder also increases significantly. Using a 4-*X*-wire three-dimentional vorticity probe, Yiu *et al.* [11] examined the Reynolds number effects on the turbulent near wake over the Re range of 2500–10000. They found that the streamwise vorticity component "jump" significantly as Re is increased from 5000 to 10 000, which coincides with that reported by Lin *et al.* [10]. Correspondingly, the contributions from the coherent structures to the spanwise vorticity variance decline appreciably, suggesting an increased three-dimentionality of the flow, which was ascribed to the generation of small-scale Kelvin-Helmholtz vortices.

Several techniques have been developed to investigate the large-scale structures in the turbulent wakes, such as the vorticity-based technique [13], window average gradient method (WAG) [14] and phase-averaging method [15,16]. However, the above mentioned methods cannot provide information on the contributions from the various scales of vortical structures to the turbulent energy, Reynolds stresses, and vorticity variances. The wavelet technique has proven to be effective to extract information on the turbulence structures at various scales (or frequencies). Wavelet transformation has the advantage of quasilocality in both physical space and Fourier space which allows extracting the time evolution of the various scales in the sampled signal. The identification of turbulence structures based on wavelet techniques has been studied by many researchers [17–21]. Recently, an orthogonal wavelet multiresolution technique was applied to the analysis of the turbulent structures of various scales in

*Email: mtmzhou@ntu.edu.sg

TABLE I. Summary of the experimental conditions on the wake centerline. U_0 is the maximum velocity deficit of the wake. $R_\lambda \equiv u'\lambda/\nu$ is the Taylor microscale Reynolds number. $\lambda \equiv u'/(du/dx)'$ is the longitudinal Taylor microscale. L is the half width of the wake. $\langle\varepsilon\rangle_{iso} \equiv 15\nu\langle(du/dx)^2\rangle$ is mean turbulent energy dissipation rate. $\eta \equiv (\nu^3/\langle\varepsilon\rangle)^{1/4}$ is the Kolmogorov length scale. $f_K \equiv U_1/2\pi\eta$ is the Kolmogorov frequency. $L_u \equiv U_1\int_0^{\tau_0}\rho_u(\tau)d\tau$ is the longitudinal integral length scale, ρ_u is the longitudinal velocity autocorrelation coefficient, τ is the time delay and τ_0 is time at which the first zero crossing occurs.

Re	U_0 (m/s)	u' (m/s)	v' (m/s)	w' (m/s)	L (mm)	$\langle\varepsilon\rangle$ (m^2 s^{-3})	η (mm)	L_u (mm)	λ (mm)	R_λ	f_K (Hz)	u_K (m/s)
2000	0.35	0.1	0.081	0.089	25.5	0.058	0.5	20.5	6.3	42	1510	0.031
4000	0.6	0.23	0.183	0.195	23	0.58	0.28	22.1	4.46	68	5220	0.055
6000	0.8	0.33	0.27	0.3	21	1.59	0.22	34.3	3.98	88	10180	0.07

the near wake of a circular cylinder by Rinoshika and Zhou [22]. It is observed for the first time that the spanwise vorticity contours of the wavelet component at the averaging frequency of Kármán vortices display a secondary spanwise structure near the saddle point in the near wake of a circular cylinder. Using the same technique, Zhou and Li [23] and Rinoshika and Zhou [24,25] further investigated the dependence of the turbulent structures of different scales on various wake-generating bodies or initial conditions in the near and far wakes. Their results indicate that the intermediate, as well as the large-scale structures, depend on the initial conditions and further suggested a dependence of the wake turbulence structure on Re. As a matter of fact, Zhou *et al.* [26] reported the dependence on Re of the large-scale turbulence structures in a turbulent far wake.

One objective of this work is to explore further the possible dependence of the far-wake turbulence on Re, in particular, focusing on the aspects of vorticity. For this purpose, a probe that is similar in design to that used by Yiu *et al.* [11] was employed to measure the three-dimensional vorticity components simultaneously. Vorticity is an important characteristic of turbulence that can provide fundamental information on multiscale turbulent structures. Therefore, the second objective is to investigate the connection between the three-component vorticity and the multiscale vortical structures, which is fundamentally important to the thorough understanding of the far-wake turbulence.

In the present study, the wavelet technique is used to decompose the measured three-component vorticity signals into a number of wavelet components based on their central frequencies, which are representative of the turbulent structures of different scales [22]. The contributions from the turbulent structures of various scales to the Reynolds stresses, velocity, and vorticity variances are evaluated. The Re dependence of the large-, intermediate-, and small-scale structures in the far wake is documented in details in terms of the three-dimensional vorticity.

II. EXPERIMENTAL DETAILS

The experiments were conducted in a closed loop wind tunnel with a test section of 1.2 m (width) $\times$ 0.8 m (height) and 2.2 m (length). The three-dimensional vorticity were measured simultaneously at three free stream velocities, i.e., 5 m/s, 10 m/s, and 15 m/s, corresponding to Re=2000, 4000, and 6000, respectively. The measurement location is at $x_1/d=240$, where d ($\equiv$6.35 mm) is the diameter of the stainless steel circular cylinder. At this location, the Kolmogorov length scales η [$\equiv(\nu^3/\langle\varepsilon\rangle)^{1/4}$] are about 0.5, 0.3, and 0.2 mm for Re=2000, 4000, and 6000, respectively, where $\langle\varepsilon\rangle_{iso} \equiv 15\nu\langle(du/dx)^2\rangle$ is mean turbulent energy dissipation rate obtained based on the isotropic assumption by applying spectral correction to $\langle(du/dx)^2\rangle$ [27]. The choice of the measurement location at $x/d=240$ is a compromise of the length of the test section of our tunnel and the Reynolds number we want to achieve in our experiments. In addition, according to the previous study by Browne and Antonia [28], the turbulent flow is approximately self-preserving at $x/d=240$ even though there were no vorticity data available to show that vorticity field is self-preserving at this location. The local turbulence intensity u_j'/U_1 (hereafter, a prime denotes rms values, u_j with $j=1$, 2, or 3 is the velocity fluctuations in the x_j direction and U_1 is the local mean velocity) for all Reynolds numbers is less than 2%, favoring the use of Taylor's hypothesis. The experimental conditions are summarized in Table I.

The probe consists of four X probes (Fig. 1). Two are in the x_1-x_2 plane and separated in the x_3 direction; the other two are in the x_1-x_3 plane and separated in the x_2 direction. The performance of this kind of probe has been previously verified by Zhu and Antonia [29] in a turbulent far wake. It is assumed that each X probe measures two velocity components at the center of the probe. The separation between the two inclined wires in each X probe is about 0.7 mm. The separations between the centers of the two X probes in x_2 and x_3 directions are about 2.7 mm. The effective angles of the two wires in each X probe are about 37°. The hot wires were etched from Wollaston (Pt-10%Rh) wires. The active lengths are about $200d_w$, where d_w is the diameter of the wires and equals to 2.5 μm. The hot wires were operated with in-house constant temperature circuits at an overheat ratio of 1.5. The probe was calibrated at the centerline of the tunnel against a Pitot-static tube. The yaw calibration was performed over ±20°. The output signals from the anemometers were passed through buck and gain circuits and low-pass filtered at the cut-off frequency f_c which is close to f_K, where $f_K \equiv U_1/2\pi\eta$ is the Kolmogorov frequency. The filtered signals were sampled at a frequency f_s of 3200 Hz, 10 400 Hz, and 18 400 Hz for 5 m/s, 10 m/s, and 15 m/s, respectively, using a 16-bit A/D converter. The sampling period is about 60 s.

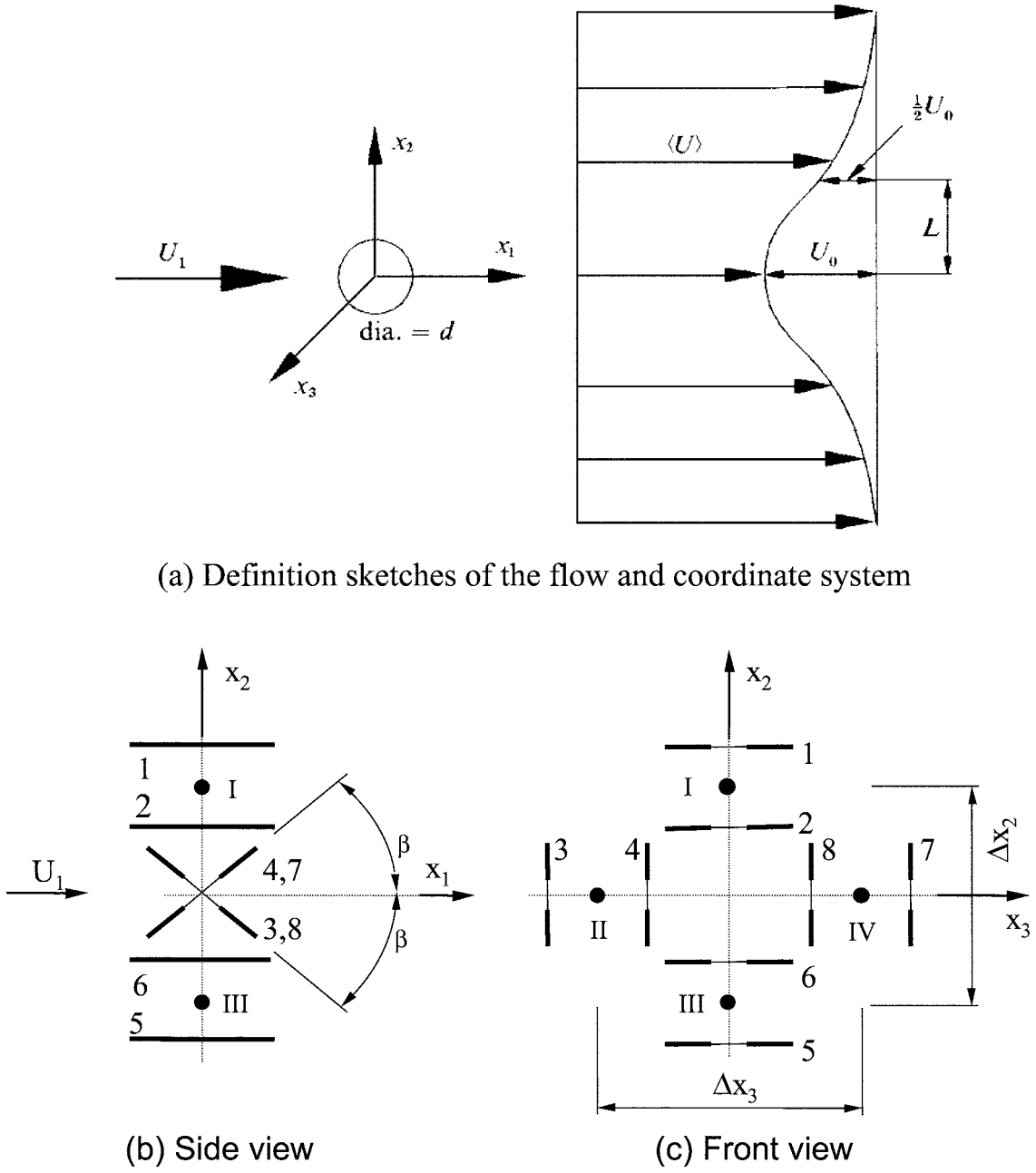

FIG. 1. Coordinate system and the sketches of the eight-wire vorticity probe.

The three vorticity components are obtained from the u_i signals measured by the vorticity probe using the following finite difference method, i.e., $\partial u_j/\partial x_l = \Delta u_j/\Delta x_l$. The streamwise derivatives are calculated using Taylor's hypothesis, i.e., $\partial u_j/\partial x_1 = -U_1^{-1}\Delta u_j/2\Delta t$ $(j=2,3)$, where Δt $(\equiv 1/f_s)$ is one sampling time interval. This method would have the advantage of keeping $\Delta x_1 \approx \Delta x_2 \approx \Delta x_3$ at the lowest speed to avoid phase shift between the velocity gradients in the expressions of vorticity components [30]. For the other two higher flow speeds, we have chosen higher values of sampling frequency so that the Kolmogorov scales can be resolved in the vorticity signals. In the latter two cases, we cannot achieve $\Delta x_1 \approx \Delta x_2 \approx \Delta x_3$. Instead, we would have $2\Delta x_1 \approx \Delta x_2 \approx \Delta x_3$. The three vorticity components can be obtained, viz.

$$\omega_1 = u_{3,2} - u_{2,3} \approx \frac{\Delta u_3}{\Delta x_2} - \frac{\Delta u_2}{\Delta x_3}, \tag{1}$$

$$\omega_2 = u_{1,3} - u_{3,1} \approx \frac{\Delta u_1}{\Delta x_3} - \frac{\Delta u_3}{\Delta x_1}, \tag{2}$$

and

$$\omega_3 = u_{2,1} - u_{1,2} \approx \frac{\Delta u_2}{\Delta x_1} - \frac{\Delta u_1}{\Delta x_2}. \tag{3}$$

Experimental uncertainties were estimated in U_1 and u_j' $(j=1,2,3$; a prime denotes the rms values) from the errors in the hot-wire calibration data as well as the scatter (20 to 1 odds) in repeating the experiments for a number of times.

The uncertainty for U_1 was about ±2%, while uncertainties for u_1', u_2', and u_3' were about ±4.5, ±5, and ±5%, respectively. The uncertainties for wire separations Δx_j were ±2% ($j=1$) and ±5% ($j=2$ and 3). Using the above estimates, the uncertainties for ω_j' ($j=1,2,3$) were estimated by the method of propagation of errors [31]. The resulting values were about ±10, ±12, and ±12% for $j=1,2,3$, respectively.

III. WAVELET MULTIRESOLUTION ANALYSIS

Wavelet transform and multiresolution analysis are discussed in detail in many references [22,32,33], and therefore only the key concepts and equations will be given in this section. The algorithm for numerically calculating the discrete wavelet transform is similar to the fast Fourier transform (FFT), and a detailed description can be found in Press *et al.* [34].

A. Discrete wavelet transform (DWT)

The one-dimensional discrete wavelet transform is defined as

$$Dv_{i,n} = \sum_m v(x^m)\Psi_{i,n}(x^m), \tag{4}$$

where $v(x)$ is the one-dimensional function and $\Psi_{i,n}(x)$ is the one-dimensional orthogonal wavelet basis, i is the wavelet level (i.e., the scale), n is the location. Here $Dv_{i,n}$ is called discrete wavelet transform coefficients. The one-dimensional orthonormal wavelet basis, $\Psi_{i,n}(x)$, is simply given by

$$\Psi_{i,n}(x) = 2^{-i/2}\psi(2^{-i}x - n). \tag{5}$$

In the present study, the Daubechies family with an order of 20 is selected as the wavelet basis. The original function can be reconstructed from the inversion of $Dv_{i,n}$, viz.

$$v(x) = \sum_i \sum_n Dv_{i,n}\Psi_{i,n}(x). \tag{6}$$

As a linear transform, the wavelet transform of a function is a vector whose elements are the wavelet transforms of the components sampled with a scale of 2^i. The high scale level of i indicates high frequency corresponding to small-scale structures and vice versa. In general, the fine-scale discrete wavelet transform can capture the local features of the original functions and provide a parsimonious representation of the functions at the same time.

B. Multiresolution analysis

Decomposition of a time series into various resolutions through an iteration process is termed as multiresolution analysis. Multiresolution analysis provides an efficient mechanism for going from one resolution to another. Mallat [32] showed that a time series $f(t)$ can be completely decomposed in terms of "approximations" and "details" relative to different time scales, which are provided by the scaling functions and wavelets, respectively. Given that the discrete wavelet transform is an orthonormal and linear transform, from Eq. (6), the function can be represented by the summation of wavelet components at different central frequencies (from low to high), viz.

$$v(x) = Mv_1 + Mv_2 + \cdots + Mv_k, \tag{7}$$

where

$$Mv_i = \sum_n Dv_{i,n}\Psi_{i,n}(x). \tag{8}$$

In Eq. (7), Mv_1 and Mv_k are the wavelet components at level 1 (the lowest frequency, coarse information) and level k (the highest frequency, detailed information), respectively. The method described in Eqs. (7) and (8) are called wavelet multiresolution analysis which is an orthonormal decomposition processing. The original function can be reconstructed by summation of all the frequency components in multiresolution analysis.

In the present study, the instantaneous velocity component $U_j(x_1,x_2,x_3,t)$ can be written as the sum of a time-averaged component $\bar{U}_j$ and a fluctuation component u_j, viz.

$$U_j = \bar{U}_j + u_j. \tag{9}$$

To extract various scales in turbulence structures, the multiresolution analysis is used to decompose the velocity fluctuation components u_j into a number of orthonormal wavelet components based on wavelet levels, which correspond to the different central frequencies and are directly linked to turbulent structure scales [21,22,24,25]. The multiresolution analysis may process fewer data by selecting relevant details that are essential to perform the extraction of multiscale flow structures, and decompose the velocity fluctuations both in Fourier and physical spaces. Each wavelet component represents the turbulent structures of a certain range of frequencies (i.e., a nonzero frequency band) so that the information of any scales contained in the original data will not be lost due to a limited number of wavelet levels. From Eq. (7), the u_j can be written as

$$u_j = \sum_{i=1}^{N} u_{i,j}, \tag{10}$$

where N is the total number of wavelet levels, and $u_{i,j}$ is the wavelet component of u_j at ith wavelet level. Equation (9) can be rewritten as

$$U_j = \bar{U}_j + \sum_{i=1}^{k} u_{i,j}. \tag{11}$$

The wavelet components of the instantaneous vorticity components $\omega_j(x_1,x_2,x_3,t)$ can be written as

$$(\omega_1)_i = (u_{3,2})_i - (u_{2,3})_i \approx \frac{(\Delta u_3)_i}{\Delta x_2} - \frac{(\Delta u_2)_i}{\Delta x_3}, \tag{12}$$

$$(\omega_2)_i = (u_{1,3})_i - (u_{3,1})_i \approx \frac{(\Delta u_1)_i}{\Delta x_3} - \frac{(\Delta u_3)_i}{\Delta x_1}, \tag{13}$$

and

$$(\omega_3)_i = (u_{2,1})_i - (u_{1,2})_i \approx \frac{(\Delta u_2)_i}{\Delta x_1} - \frac{(\Delta u_1)_i}{\Delta x_2}. \quad (14)$$

IV. RESULTS AND DISCUSSION

A. Spectra of the measured velocity signals

Figure 2 shows the spectra ϕ_{u_1} and ϕ_{u_2} on the wake centerline for the free stream velocities of 5 m/s, 10 m/s, and 15 m/s, respectively. The spectrum ϕ_{u_1} is defined such that $\int_{-\infty}^{\infty}\phi_\alpha^*(k_1^*)dk_1^* = \langle \alpha^{*2} \rangle$. Hereafter, a superscript asterisk represents normalization by Kolmogorov scales η and u_K. Turbulent scales corresponding to the longitudinal integral length scale $L_u \equiv U_1 \int_0^{\tau_0} \rho_u(\tau) d\tau$ and the longitudinal Taylor microscale $\lambda \equiv u'/(du/dx)'$ are also indicated in the figure. While there is no pronounced peaks in the distributions of ϕ_{u_1}, there exist peaks in the distributions of ϕ_{u_2} at frequencies of 60 Hz, 105 Hz, and 180 Hz for Re=2000, 4000, and 6000, respectively. The peaks become more apparent as Re increases. These frequencies correspond to a Strouhal number St ($\equiv fd/U_\infty$) of about 0.07, which indicates the passage of the organized vortical structures. These corresponding frequencies will therefore be used as the basic frequencies f_0 in the wavelet analysis to represent the large-scale vortical structures.

B. Contributions to Reynolds shear stress, velocity and vorticity variances from different wavelet components at Re of 4000

In this section, results and discussion will be focused on the measurements at the velocity of 10 m/s (i.e., Re=4000) to study the contributions to Reynolds shear stress, velocity and vorticity variances from different wavelet components. In order to examine the turbulent structures at various scales, the velocity fluctuations $u_j(x_1, x_2, x_3, t)$ are decomposed into a number of orthonormal wavelet components based on wavelet levels, which correspond to the central frequencies $f_0/4$, $f_0/2$, f_0, $2f_0$, $4f_0$, $8f_0$, $16f_0$, and $32f_0$, and are directly linked to the scales of the turbulent structures. Turbulence structures with frequencies smaller and equal to f_0 represent large-scale structures while those at multiple of f_0 represent the intermediate and smaller scale structures.

Figure 3 shows the distributions of time-averaged velocity variances and Reynolds shear stress at different transverse locations x_2^+ obtained from the vector wavelet multiresolution analysis for different central frequencies. Hereafter the superscript + denotes normalization by the wake half width L and the local maximum velocity deficit U_0. The values of $\langle \beta\gamma \rangle_i$ are normalized by the maximum value of $\langle \beta\gamma \rangle_{\max}$, where β or γ may each represent u_1, u_2, u_3, or u_1u_2 and $\langle \beta\gamma \rangle_i$ represents the wavelet component at ith level, so that the contribution from different central frequencies can be evaluated. The measured values of $\langle \beta\gamma \rangle / \langle \beta\gamma \rangle_{\max}$ are also included in the figures. From Fig. 3, it can be seen that the values of $\langle \beta\gamma \rangle_i / \langle \beta\gamma \rangle_{\max}$ decrease for turbulent structures with different wavelet scales when the wake edge is approached. At the central frequency of f_0, the maximum values of

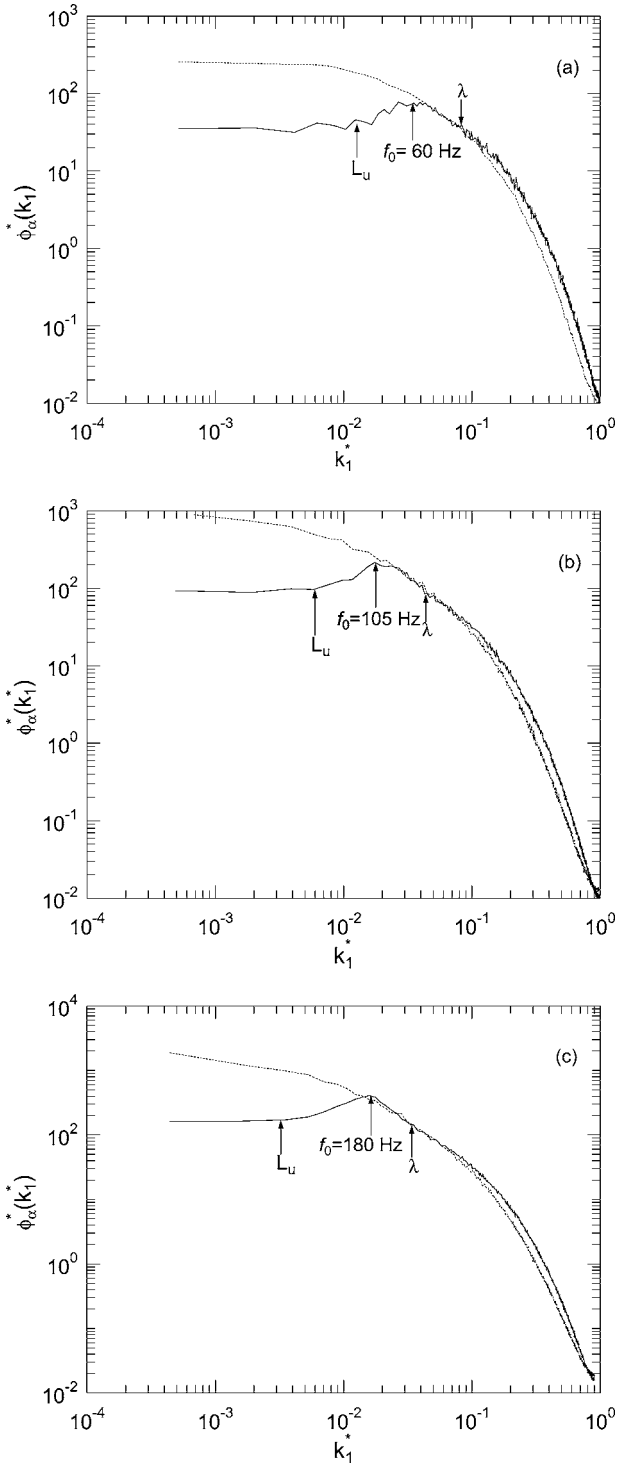

FIG. 2. Comparison of measured $\phi_{u_1}^*$ and $\phi_{u_2}^*$ on the wake centerline at different Re. - - -, $\phi_{u_1}^*$; —, $\phi_{u_2}^*$. Scales corresponding to L_u and λ are also shown. (a) Re=2000; (b) 4000; (c) 6000.

$\langle u_j^2 \rangle_{f_0} / \langle u_j^2 \rangle_{\max}$ (where j represents any one of the three velocity components) are 20.9%, 25.8%, and 22.9% for $j=1$, 2, and 3, respectively, and 30.5% for $\langle u_1 u_2 \rangle_{f_0} / \langle u_1 u_2 \rangle_{\max}$. These results are consistent with those reported by Zhou and Li [23], who showed that the maximum coherent contribution from the large-scale vortical structures with the central frequency f_0 is between 20% and 30% in the far wake behind a

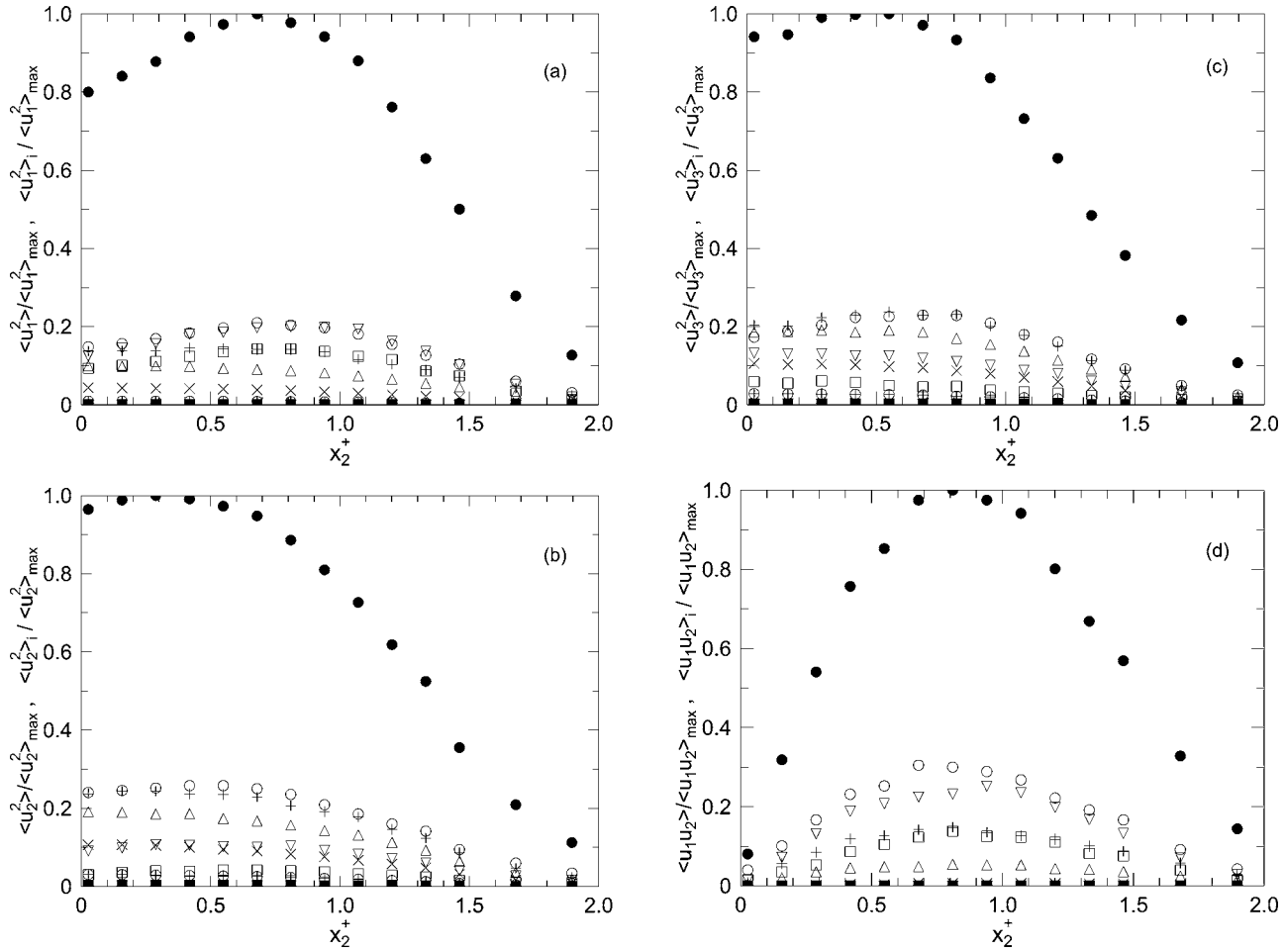

FIG. 3. Velocity variances and Reynolds shear stress of the measured and the wavelet components at various central frequencies for Re=4000. (a) $\langle u_1^2\rangle/\langle u_1^2\rangle_{\max}$ and $\langle u_1^2\rangle_i/\langle u_1^2\rangle_{\max}$; (b) $\langle u_2^2\rangle/\langle u_2^2\rangle_{\max}$ and $\langle u_2^2\rangle_i/\langle u_2^2\rangle_{\max}$; (c) $\langle u_3^2\rangle/\langle u_3^2\rangle_{\max}$ and $\langle u_3^2\rangle_i/\langle u_3^2\rangle_{\max}$; (d) $\langle u_1u_2\rangle/\langle u_1u_2\rangle_{\max}$ and $\langle u_1u_2\rangle_i/\langle u_1u_2\rangle_{\max}$. ●, measured; □, $f_0/4$; ▽, $f_0/2$; ○, f_0; +, $2f_0$; △, $4f_0$; ×, $8f_0$; ⊕, $16f_0$; ■, $32f_0$.

triangular cylinder ($x_1/d=220$). It is also observed that the values of $\langle\beta\gamma\rangle_i/\langle\beta\gamma\rangle_{\max}$ tend to be largest at f_0 for all locations of x_2^+ and decrease as the frequency increases, indicating that lower frequency eddies contain more energy than the higher frequency ones. It should be noted in Figs. 3(b) and 3(c) that, the decreases of $\langle u_2^2\rangle$ and $\langle u_3^2\rangle$ are rather small when the central frequency increases from f_0 to $2f_0$, and the wavelet components corresponding to these two frequencies contribute most to $\langle u_2^2\rangle$ and $\langle u_3^2\rangle$. This result indicates that there is a significant contribution to the time-averaged transverse and spanwise velocity variances from the intermediate-scale structures, which is consistent with that revealed by Fig. 2. In Fig. 3, it is also observed that when the central frequency is larger than $4f_0$, the values of $\langle\beta\gamma\rangle_i/\langle\beta\gamma\rangle_{\max}$ drop quickly with the increase of the central frequencies.

The distributions of the time-averaged three vorticity variances, obtained from the wavelet multiresolution analysis at different wavelet levels or central frequencies are shown in Fig. 4. The values of $\langle\omega_j^2\rangle_i$ are normalized by the maximum value of $\langle\omega_j^2\rangle_{\max}$ to indicate the contribution from different central frequencies, where j ($\equiv$1, 2, or 3) represents any component of the vorticity vector and $\langle\omega_j^2\rangle_i$ represent the wavelet components at ith level. The measured vorticity variances $\langle\omega_j^2\rangle$ are also included in the figure for comparison. It can be seen in each figure that, both $\langle\omega_j^2\rangle/\langle\omega_j^2\rangle_{\max}$ and $\langle\omega_j^2\rangle_i/\langle\omega_j^2\rangle_{\max}$ drop when the free stream is approached. It needs to be noted that the maximum value of $\langle\omega_1^2\rangle_i/\langle\omega_1^2\rangle_{\max}$, corresponding to central frequency of f_0 [Fig. 4(a)], accounts for about 13% of the maximum longitudinal vorticity variance for $x_2^+<1$. This value is much larger than that for $\langle\omega_2^2\rangle_i/\langle\omega_2^2\rangle_{\max}$ [7.4%, Fig. 4(b)] and $\langle\omega_3^2\rangle_i/\langle\omega_3^2\rangle_{\max}$ [8.9%, Fig. 4(c)], indicating a relatively larger contribution to the longitudinal total vorticity variance from the large-scale structures than both to the transverse and to the spanwise vorticity components. This result is consistent with the spectra of the three vorticity components on the wake centerline, as shown in Fig. 5.

The spectrum of ω_1 contains more energy than the other two vorticity components for low and moderate frequencies (e.g., $f\leqslant 300$ Hz), implying that the large-scale structures contribute more to the longitudinal vorticity component than both to the transverse and to the spanwise vorticity components. The present result is different from the observation in the near wake ($x_1/d=10$) behind a circular cylinder [35], where a relatively larger contribution to the total spanwise vorticity variance from the large-scale structures is found. This result seems to suggest that as the vortical structures

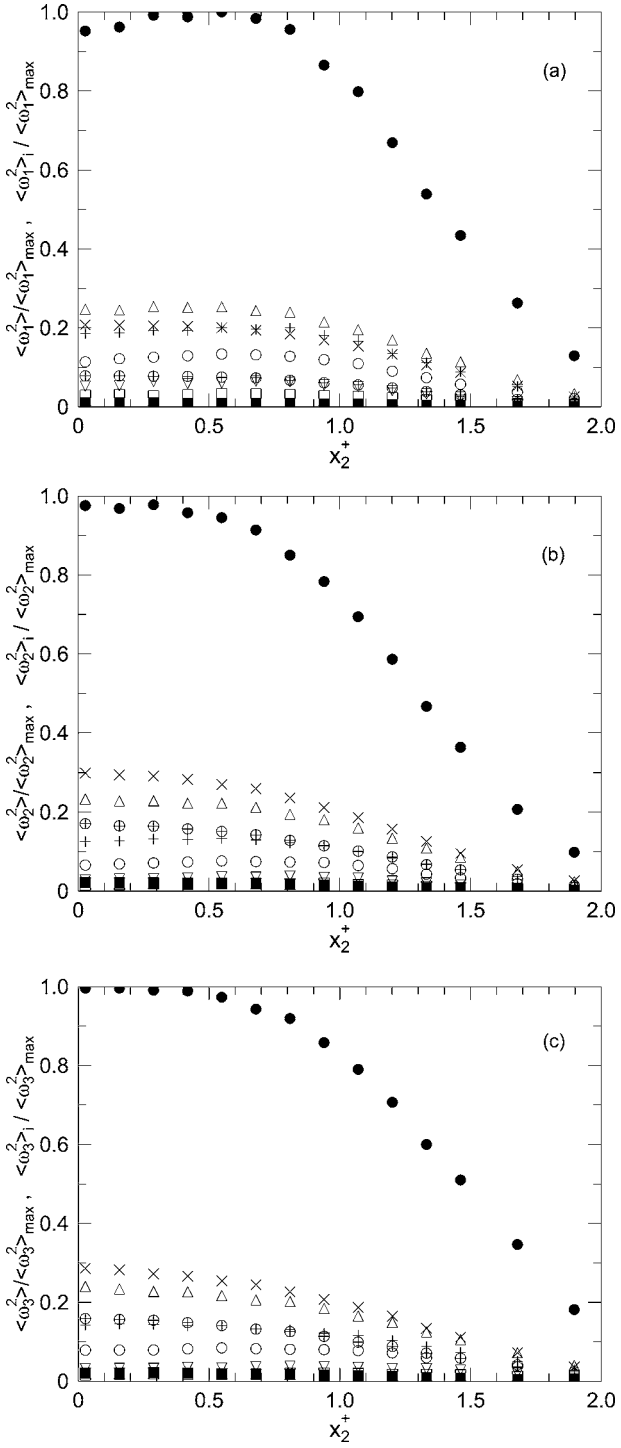

FIG. 4. Vorticity variances of the measured and the wavelet components at various central frequencies for Re=4000. (a) $\langle\omega_1^2\rangle/\langle\omega_1^2\rangle_{\max}$ and $\langle\omega_1^2\rangle_i/\langle\omega_1^2\rangle_{\max}$; (b) $\langle\omega_2^2\rangle/\langle\omega_2^2\rangle_{\max}$ and $\langle\omega_2^2\rangle_i/\langle\omega_2^2\rangle_{\max}$; (c) $\langle\omega_3^2\rangle/\langle\omega_3^2\rangle_{\max}$ and $\langle\omega_3^2\rangle_i/\langle\omega_3^2\rangle_{\max}$. ●, measured; □, $f_0/4$; ▽, $f_0/2$; ○, f_0; +, $2f_0$; △, $4f_0$; ×, $8f_0$; ⊕, $16f_0$; ■, $32f_0$.

evolve downstream, the spanwise and rib-like structures show different contributions to the three vorticity components. Compared with Fig. 3, Fig. 4 shows that, the turbulent structures with higher central frequencies tend to contribute more to the vorticity variances than those of lower ones since $\langle\omega_1^2\rangle_i/\langle\omega_1^2\rangle_{\max}$ is largest at $4f_0$, while the contributions to

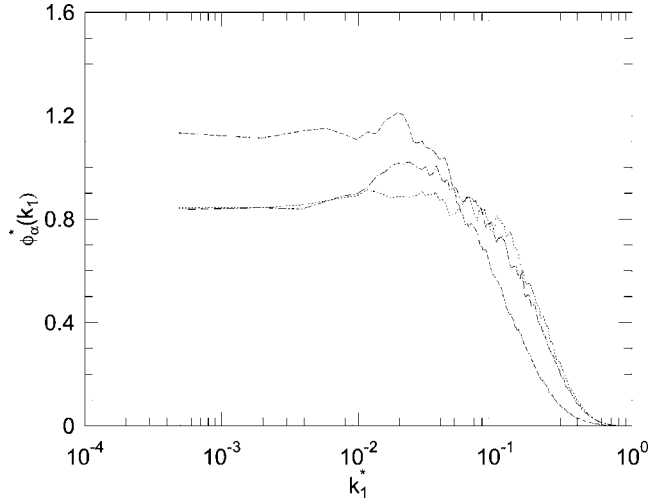

FIG. 5. Comparison of measured spectra of ω_1, ω_2, and ω_3 on the wake centerline at Re=4000. – –, ω_1; - - -, ω_2; – – –, ω_3.

$\langle\omega_2^2\rangle_i/\langle\omega_2^2\rangle_{\max}$ and $\langle\omega_3^2\rangle_i/\langle\omega_3^2\rangle_{\max}$ are dominated by structures with central frequency of $8f_0$. In Figs. 4(b) and 4(c), it can be seen that within the half width, contributions at $2f_0$, $4f_0$, $8f_0$, and $16f_0$ are all higher than that corresponding to f_0 for all three vorticity components. Figure 6 shows the total contributions from the intermediate- and relatively small-scale structures with central frequencies of $2f_0$, $4f_0$, $8f_0$, and $16f_0$. It shows that on the wake centerline, the total contribution from the included subsets ($2\sim16f_0$) takes about 84.6% of $\langle\omega_2^2\rangle_{\max}$ and $\langle\omega_3^2\rangle_{\max}$, and 72.6% for $\langle\omega_1^2\rangle_{\max}$, indicating that more transverse and spanwise vorticity resides in the intermediate and small-scale structures than the longitudinal vorticity. In addition, this result is consistent with the previous perception that, compared with the large-scale turbulent structures (with central frequencies lower than $2f_0$), the intermediate and relatively small-scale structures contribute more to vorticity.

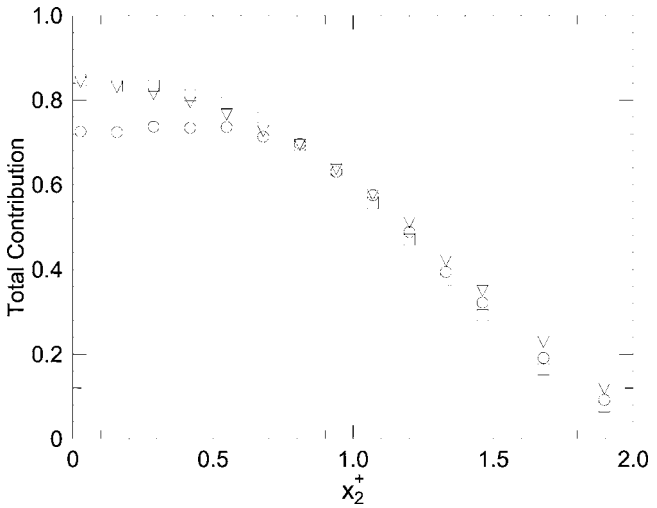

FIG. 6. The total contributions to vorticity variance from the wavelet components of $2f_0$, $4f_0$, $8f_0$, and $16f_0$ at Re=4000. ○, $\langle\omega_1^2\rangle_i/\langle\omega_1^2\rangle_{\max}$; □, $\langle\omega_2^2\rangle_i/\langle\omega_2^2\rangle_{\max}$; ▽, $\langle\omega_3^2\rangle_i/\langle\omega_3^2\rangle_{\max}$.

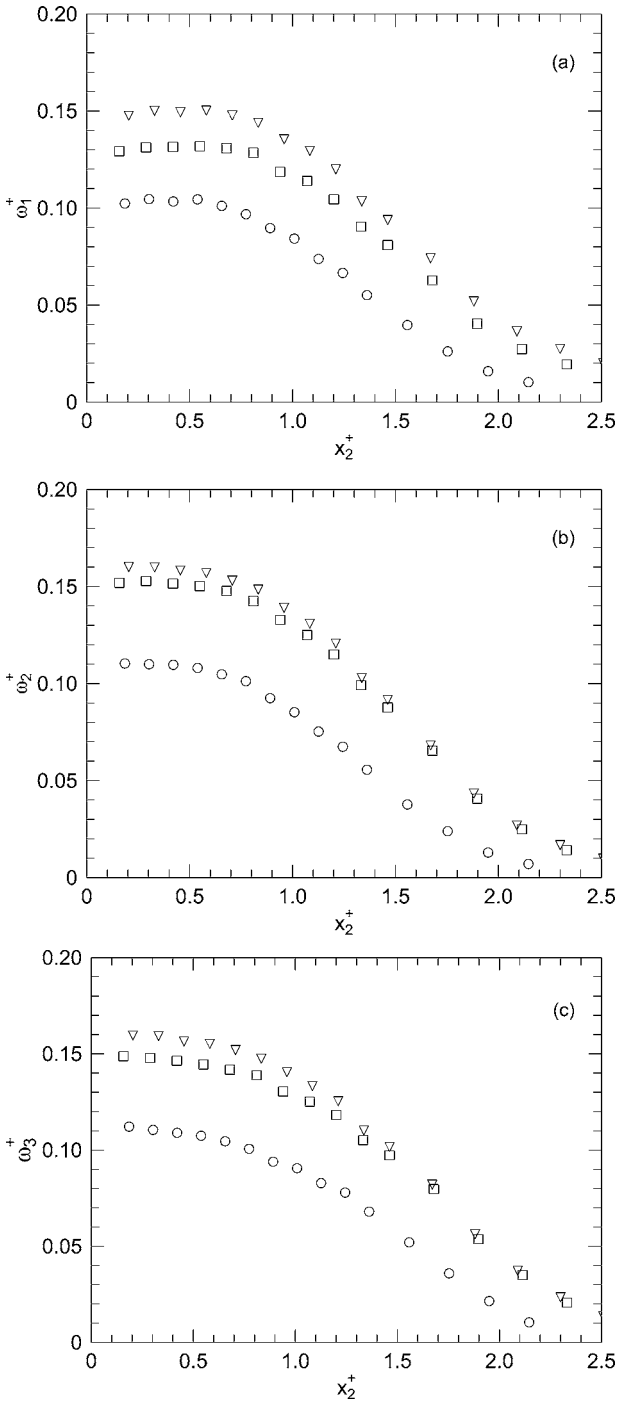

FIG. 7. Distributions of the corrected rms values of the vorticity components across the wake. (a) ω_1; (b) ω_2; (c) ω_3. ○, Re=2000; □, 4000; ▽, 6000.

C. Reynolds number effect on the contributions to vorticity variances from different wavelet components

Before presenting the wavelet analysis of Reynolds number effect on vorticity components, Fig. 7 shows the corrected rms values of the three vorticity components across the wake at Re=2000, 4000, and 6000, respectively. Due to the limitation of spatial resolution of the vorticity probe, the high wave number part of the vorticity spectra are expected to be attenuated. The spectral attenuation, however, can be corrected by assuming local isotropy. Details of the correction procedures and expressions for spectral attenuation can be found in Zhu and Antonia [36]. In turbulent far wake flows, local isotropy has been approximately verified in the region of $x_2^+ \leqslant 1$ [37]. The scaling of the rms values of ω_j is based on L, U_0, and R_L ($\equiv LU_0/\nu$) as suggested by Antonia *et al.* [38] to account for the Reynolds number effect, i.e.

$$\omega_j^+ = \omega_j' \frac{L}{U_0} R_L^{-1/2}, \tag{15}$$

where ω_j^+ denotes the normalized rms values of ω_j. On the wake centerline, the magnitude of ω_1^+ [Fig. 7(a)] is increased by 30% and 15% when Re is changed from 2000 to 4000 and from 4000 to 6000, respectively. The corresponding increases are 40% and 7% for ω_2^+ [Fig. 7(b)], and 34% and 8% for ω_3^+ [Fig. 7(c)]. The above increases of the rms values of the three vorticity components with Re may indicate that vorticity is generated in a sudden "jump" way when Reynolds number is changed from 2000 to 4000. The Reynolds number effect on vorticity generation declines significantly when Re is changed from 4000 to 6000. This trend is consistent with that reported by Yiu *et al.* [11] in the turbulent near wakes and may indicate the "memory" effect of turbulence on Reynolds number in the far wake.

Figures 8–13 show the vorticity variances of the wavelet components at the central frequencies $f_0/2$, f_0, $2f_0$, $4f_0$, $8f_0$, and $16f_0$. The structures with frequencies lower than $f_0/2$ and higher than $16f_0$ are not calculated, since as shown in Fig. 4, the structures with central frequencies of $f_0/4$ and $32f_0$ contribute least to the total energy with a percentage being smaller than 3%. Figures 8 and 9 show the vorticity variances from the wavelet components at the central frequencies of $f_0/2$ and f_0, which represent the large-scale structures. Similar variations with Re are found in the two figures for individual vorticity component. In Fig. 8 ($f_0/2$), when $x_2^+ < 1.5$, the wavelet contributions decrease with the increase of Re. For example, $\langle\omega_1^2\rangle_i/\langle\omega_1^2\rangle_{\max}$, $\langle\omega_2^2\rangle_i/\langle\omega_2^2\rangle_{\max}$, and $\langle\omega_3^2\rangle_i/\langle\omega_3^2\rangle_{\max}$ decrease by about 2.3%, 3%, and 1.5% when Re is changed from 2000 to 4000. The corresponding decreases of the three vorticity components at f_0 (Fig. 9) are 3%, 5.4%, and 2.6%, respectively. At these two central frequencies, the changes of the wavelet contributions to $\langle\omega_2^2\rangle_i/\langle\omega_2^2\rangle_{\max}$ and $\langle\omega_3^2\rangle_i/\langle\omega_3^2\rangle_{\max}$ when Reynolds number is increased from 4000 and 6000 (Fig. 9) are too small to draw any firm conclusion, except for $\langle\omega_1^2\rangle_i/\langle\omega_1^2\rangle_{\max}$, which decreases by about 1.8% [Fig. 8(a)] and 2% [Fig. 9(a)], respectively.

The contributions to vorticity variances from structures with central frequencies of $2f_0$ and $4f_0$, which mainly represent the intermediate scale turbulent structures, are shown in Figs. 10 and 11. It can be seen that, for $x_2^+ < 1.5$, the contributions to $\langle\omega_1^2\rangle$, $\langle\omega_2^2\rangle$, and $\langle\omega_3^2\rangle$ at $2f_0$ (Fig. 10) decrease by about 5.5%, 8.3%, and 3.4%, respectively, when Re increases from 2000 to 4000. At central frequency of $4f_0$ (Fig. 11), the decrease of contributions is about 7.7% for $\langle\omega_2^2\rangle$ when Re increases from 2000 to 4000. In contrast to $\langle\omega_2^2\rangle_i$, the decreases of $\langle\omega_1^2\rangle_i$ and $\langle\omega_3^2\rangle_i$ are much smaller, which are

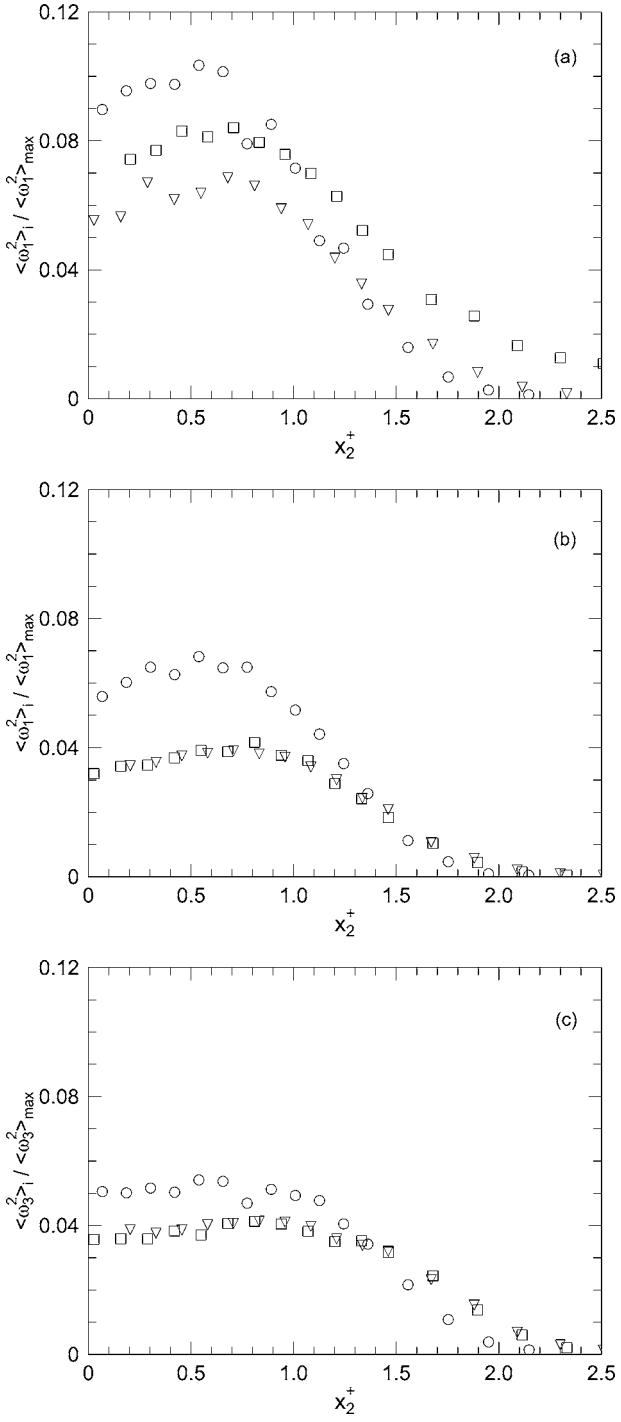

FIG. 8. Vorticity variances of the wavelet components at central frequency of $f_0/2$. (a) ω_1; (b) ω_2; (c) ω_3. ○, Re=2000; □, 4000; ▽, 6000.

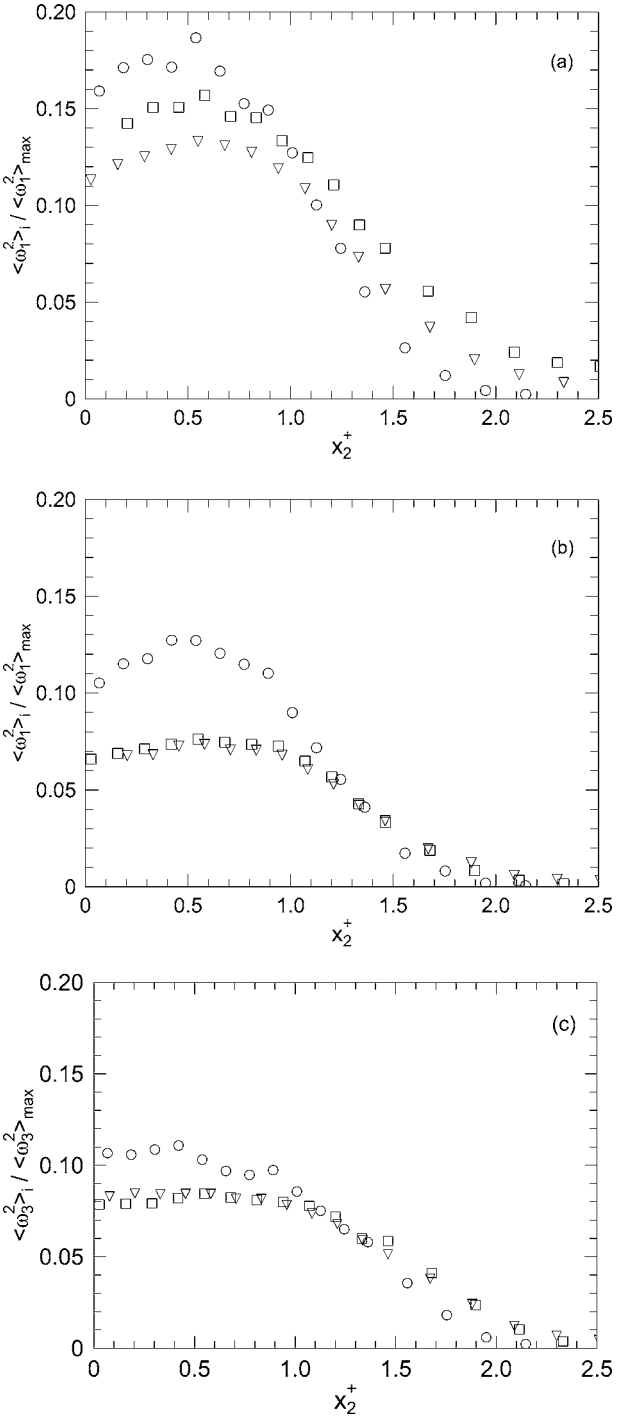

FIG. 9. Vorticity variances of the wavelet components at central frequency of f_0. (a) ω_1; (b) ω_2; (c) ω_3. ○, Re=2000; □, 4000; ▽, 6000.

about −1.6% and 0.9%, respectively. The negative or small decreases of the contributions to the longitudinal and spanwise vorticity variances may imply the appearance of the quasi-two-dimensional longitudinal and spanwise vortex structures as Re increases. This can also be inferred from the results for the central frequency of $2f_0$ (Fig. 10), at which the decreases of the contributions to longitudinal (5.5%) and spanwise vorticity (3.4%) are both smaller than that to transverse vorticity component (8.3%). In triangular cylinder and screen far wakes, Zhou and Li [23] observed the occurrence of longitudinal rib-like structures in the saddle regions which occur between successive spanwise structures. As a matter of fact, the generation of the intermediate scale structures is essential to form the inertial scale subrange of the high Reynolds number flows. The decreases of the wavelet contributions to the three-component vorticity variances at the central frequency $4f_0$ are too small to draw any firm conclusion when Reynolds number is changed from 4000 to 6000.

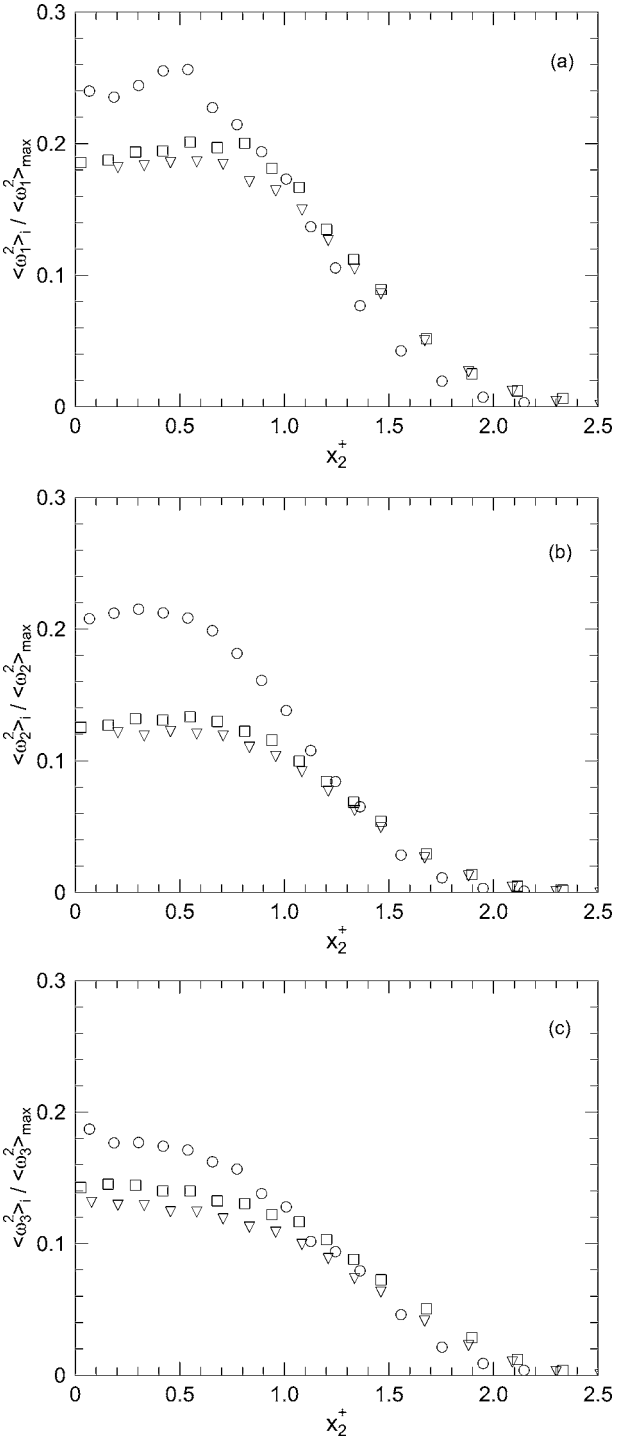

FIG. 10. Vorticity variances of the wavelet components at central frequency of $2f_0$. (a) ω_1; (b) ω_2; (c) ω_3. ○, Re=2000; □, 4000; ▽, 6000.

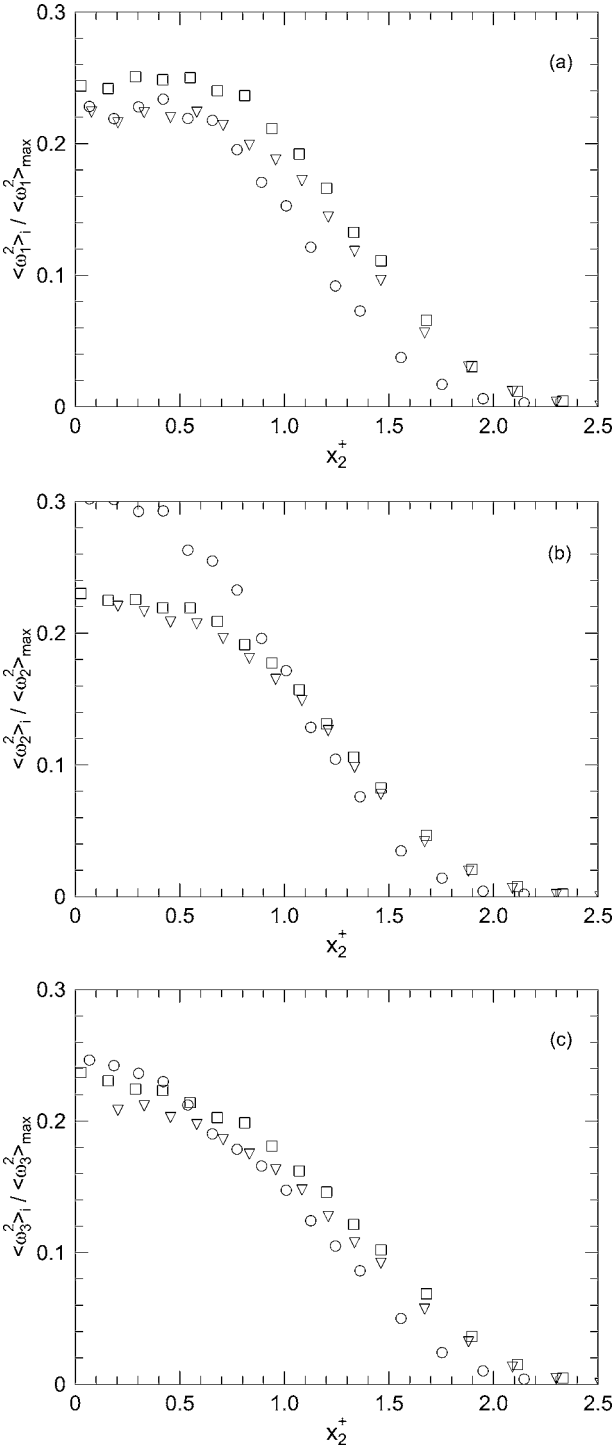

FIG. 11. Vorticity variances of the wavelet components at central frequency of $4f_0$. (a) ω_1; (b) ω_2; (c) ω_3. ○, Re=2000; □, 4000; ▽, 6000.

The contributions to vorticity variances at central frequencies of $8f_0$ and $16f_0$, which mainly represent the small-scale structures, are shown in Figs. 12 and 13. For $x_2^+<2$, significant increases or jump of contributions to the three vorticity components are observed when Re is changed from 2000 to 4000, indicating a strong positive Re dependence over the present Re range (2000–4000). In Fig. 12 ($8f_0$), the increases of the contributions to $\langle\omega_1^2\rangle$, $\langle\omega_2^2\rangle$, and $\langle\omega_3^2\rangle$ are 10.1%, 12%, and 13.5%, respectively. The corresponding increases are also significant at $16f_0$ (Fig. 13), which are 6.2%, 16.3%, and 13.7%. On the other hand, the changes of the wavelet contributions to the three vorticity components when Re is increased from 4000 to 6000 are not apparent. With the caveat of the experimental uncertainty associated with vorticity measurements, the changes of the wavelet contributions when Reynolds number is increased from 2000 to 4000 are

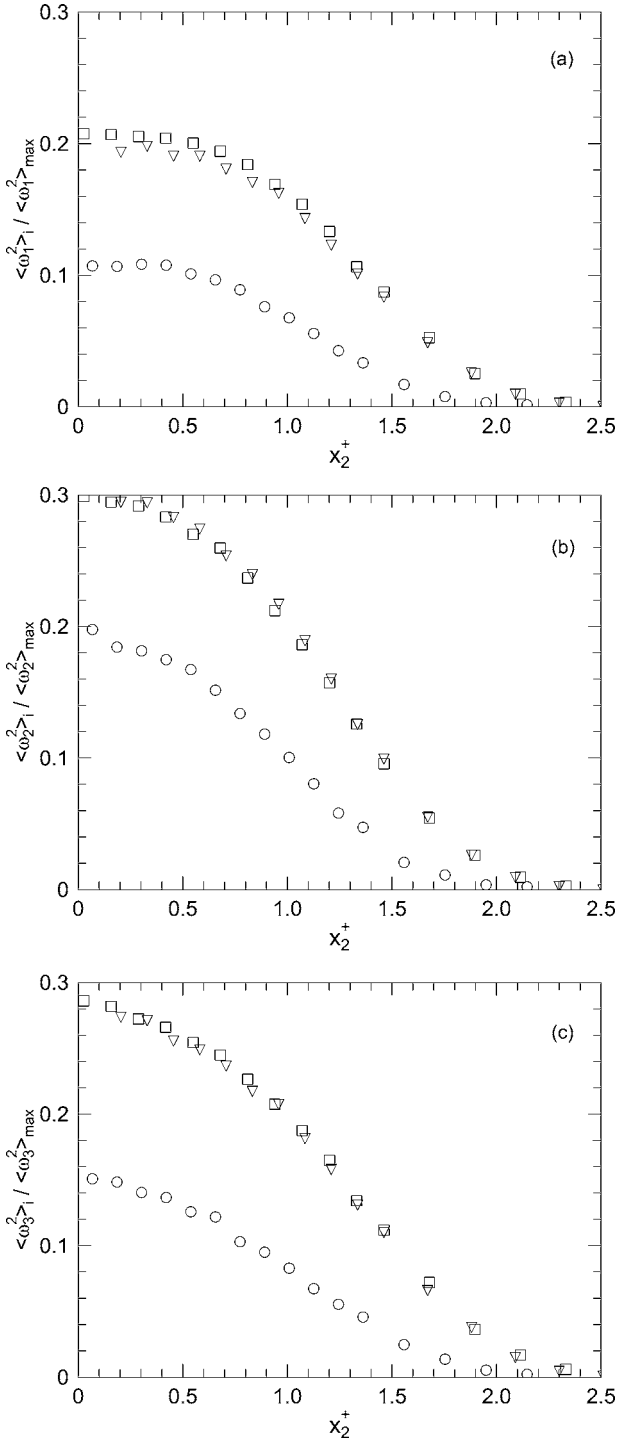

FIG. 12. Vorticity variances of the wavelet components at central frequency of $8f_0$. (a) ω_1; (b) ω_2; (c) ω_3. ○, Re=2000; □, 4000; ▽, 6000.

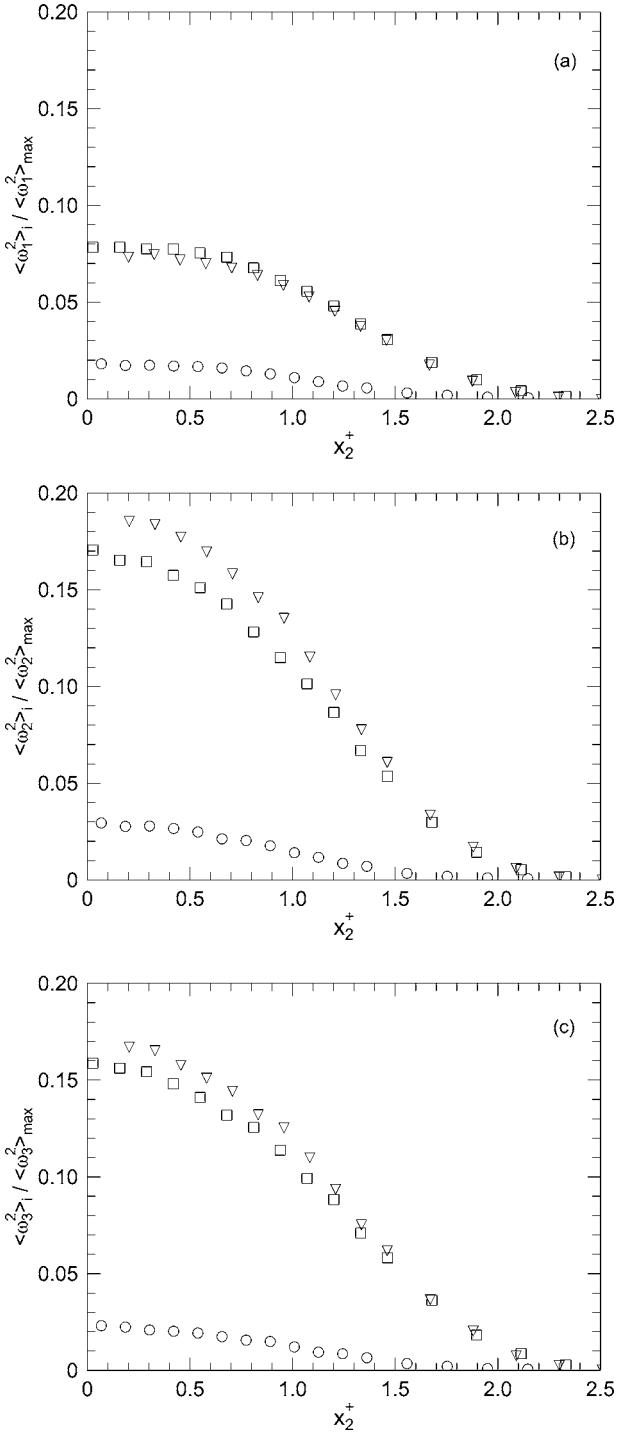

FIG. 13. Vorticity variances of the wavelet components at central frequency $16f_0$. (a) ω_1; (b) ω_2; (c) ω_3. ○, Re=2000; □, 4000; ▽, 6000.

still appreciable. The sudden jump of the contributions to vorticity variances from the turbulent structures with the central frequencies of $8f_0$ and $16f_0$ when Re is increased from 2000 to 4000 is probably due to the generation of small-scale structures at Re=4000 in the near field (Yiu *et al.* [11]), which is persistent in the far field. This result indicates that the vorticity field in the wake depends not only on the initial conditions (e.g., [39]), but also on the Reynolds numbers, which reveals the memory effects to the Reynolds number change in the near field.

V. CONCLUSIONS

All three components of the vorticity vector in the far region of a circular cylinder wake ($x_1/d=240$) were mea-

sured simultaneously by employing an eight hot-wire vorticity probe. Using the wavelet multiresolution technique, contributions to Reynolds shear stress, velocity and vorticity variances from different wavelet components are evaluated. The maximum coherent contribution to velocity variances and Reynolds shear stress from the large-scale vortical structures with the central frequency of f_0 is between 20% and 30%, which is consistent with those reported by Zhou and Li [23].

The present results at Re=2000 show that the large-scale structures (with central frequency f_0) contribute appreciably (13%) to the longitudinal vorticity variance for $x_2^+ < 1$. In contrast, they contribute only about 7.4% to $\langle \omega_2^2 \rangle / \langle \omega_2^2 \rangle_{\max}$ and 8.9% to $\langle \omega_3^2 \rangle / \langle \omega_3^2 \rangle_{\max}$. This result indicates a relatively large contribution to the longitudinal vorticity variance from the large-scale structures than both to the transverse and to the spanwise vorticity components. The dominant contributions to the vorticity variances are from the intermediate and small-scale structures with central frequencies of $2f_0$, $4f_0$, $8f_0$, and $16f_0$, which takes about 84.6% for $\langle \omega_2^2 \rangle_{\max}$ and $\langle \omega_3^2 \rangle_{\max}$, and 72.6% for $\langle \omega_1^2 \rangle_{\max}$, indicating that vorticity resides mainly in the small-scale structures. The contributions from the large and intermediate scale structures to the vorticity variances decrease as Re increases from 2000 to 4000, while the changes of the wavelet contributions are not apparent when Re is increased from 4000 to 6000 (Figs. 8–13). There is a rapid increase in the contributions to the vorticity variances from the turbulent structures of $8f_0$ and $16f_0$, which represent the small scale turbulence structures (Figs. 12 and 13), as Reynolds number is increased from 2000 to 4000. This change echoes the observation in the near field [11], which was ascribed to the generation of small-scale structures at $\mathrm{Re} \approx 5000$. The present result could suggest a persistence of turbulent near-field structures of relatively small scales in the far field.

[1] N. A. Ahmed and D. J. Wagner, AIAA J. **41**, 542 (2003).
[2] P. M. Bevilaqua and P. S. Lykoudis, J. Fluid Mech. **80**, 589 (1978).
[3] I. Wygnanski, F. Champagne, and B. Marasli, J. Fluid Mech. **168**, 31 (1986).
[4] Y. Zhou and R. A. Antonia, Exp. Fluids **19**, 112 (1995).
[5] J. P. Bonnet, J. Delville, and H. Garem, Exp. Fluids **4**, 189 (1986).
[6] W. K. George, in *Advances in Turbulence*, edited by W. K. George and R. Arndt (Springer, Berlin, 1989), p. 39.
[7] J. H. Gerrard, J. Fluid Mech. **25**, 143 (1966).
[8] M. M. Zdravkovich, Int. Colloquium on Bluff-Body Aerodynamics and Its Applications, Kyoto, Japan, Oct. 17–20 (1988).
[9] B. Cantwell and D. Coles, J. Fluid Mech. **136**, 321 (1983).
[10] J. C. Lin, J. Towfighi, and D. Rockwell, J. Fluids Struct. **9**, 409 (1995).
[11] M. W. Yiu, Y. Zhou, T. Zhou, and L. Cheng AIAA J. **42**, 1009 (2004).
[12] A. Roshko, NACA Rep **1191**, 124 (1954).
[13] A. K. M. F. Hussain and M. Hayakawa, J. Fluid Mech. **180**, 193 (1987).
[14] H. J. Zhang, Y. Zhou, and R. A. Antonia, Phys. Fluids **12**, 2954 (2000).
[15] M. Kiya and M. Mutsumura, J. Fluid Mech. **190**, 343 (1988).
[16] Y. Zhou, H. J. Zhang, and M. W. Yiu, J. Fluid Mech. **458**, 303 (2002).
[17] C. Meneveau, J. Fluid Mech. **232**, 469 (1991).
[18] H. Li, J. Fluids Eng. **120**, 778 (1998).
[19] M. Farge, K. Schneider, and N. Kevlahan, Phys. Fluids **11**, 2187 (1999).
[20] C. Schram and M. L. Riethmuller, Meas. Sci. Technol. **12**, 1413 (2001).
[21] H. Li, H. Hu, T. Kobayashi, T. Saga, and N. Taniguchi, AIAA J. **40**, 1037 (2002).
[22] A. Rinoshika and Y. Zhou, J. Fluid Mech. **524**, 229 (2005).
[23] Y. Zhou and H. Li, Exp. Therm. Fluid Sci. **27**, 629 (2003).
[24] A. Rinoshika and Y. Zhou, Phys. Rev. E **71**, 046303 (2005).
[25] A. Rinoshika and Y. Zhou, (2005), Int. J. Heat Fluid Flow (submitted).
[26] Y. Zhou, R. A. Antonia and W. K. Tsang, Exp. Fluids **25**, 118 (1998).
[27] R. A. Antonia and J. Mi, J. Fluid Mech. **250**, 531 (1993).
[28] L. W. B. Browne and R. A. Antonia, Phys. Fluids **29**, 709 (1986).
[29] Y. Zhu and R. A. Antonia, Exp. Fluids **27**, 21 (1999).
[30] J. M. Wallace and J. F. Foss, Annu. Rev. Fluid Mech. **27**, 469 (1995).
[31] R. J. Moffat, Exp. Therm. Fluid Sci. **1**, 3 (1988).
[32] S. Mallat, IEEE Trans. Pattern Anal. Mach. Intell. **11**(7), 674 (1989).
[33] P. S. Addison, *The Illustrated Wavelet Transform Handbook: Applications in Science, Engineering, Medicine, and Finance*, (Institute of Physics Publishing, Bristol, 2002).
[34] W. H. Press, S. H. Teukolsky, W. T. Vetterling, and B. Flannery, *Numerical Recipes in FORTRAN (The Art of Scientific Computing)*, 2nd ed. (Cambridge University Press, Cambridge, 1992).
[35] T. Zhou, H. Li, Y. Zhou, L. P. Chua, and Z. Hao, Proceedings of the Fourth International Conference on Fluid Mechanics, Dalian, China, July 20–23 (2004).
[36] Y. Zhu and R. A. Antonia, Meas. Sci. Technol. **7**, 1492 (1996).
[37] Z. Hao, T. Zhou, L. P. Chua, and S. C. M. Yu (unpublished).
[38] R. A. Antonia, Y. Zhu, and H. S. Shafi, J. Fluid Mech. **323**, 173 (1996).
[39] R. A. Antonia and J. Mi, Exp. Therm. Fluid Sci. **17**, 277 (1998).